aerospace

MDPI

Article

A Geospatial Decision-Support Framework for Deployment of Low-Power Radar Networks for U-Space Surveillance and EMF Constraints

Fausta Mattei [1,*], Vincenzo Donato [2], Claudia Conte [2], Giancarlo Rufino [2] and Domenico Accardo [2]

[1] Centro Servizi Metrologici e Tecnologici Avanzati (CeSMA), Università degli Studi di Napoli Federico II, 80146 Naples, Italy
[2] Department of Industrial Engineering, Università degli Studi di Napoli Federico II, 80125 Naples, Italy; vincenzo.donato@unina.it (V.D.); claudia.conte2@unina.it (C.C.); giancarlo.rufino@unina.it (G.R.); domenico.accardo@unina.it (D.A.)
* Correspondence: fausta.mattei@unina.it

Abstract

This work addresses the problem of planning low-power ground radar networks for surveillance in urban airspace for Advanced Air Mobility, with a focus on complex contexts such as ports, intermodal hubs, energy plants, and airport perimeters. The proposed approach introduces a continuous, deployment-oriented surrogate sensing model, used to compute a normalized detection score for non-cooperative Unmanned Aerial Vehicles within the surveillance area. The methodology integrates operational and environmental constraints using polygons that represent eligible installation areas and priority interest zones to ensure that sensor placement reflects both siting feasibility and the relative value of monitored areas. The framework also includes a first-order electromagnetic exposure-screening layer to support early-stage visualization and comparison across scenarios. Regulatory limits are not enforced in the current optimization. The development includes an interactive geospatial interface, which supports the definition of realistic scenarios and the selection of candidate radar deployment configurations consistent with user-defined siting constraints and exposure-screening assumptions.

Keywords: advanced air mobility; U-space surveillance; radar network design; surrogate sensing model; sensor placement; coverage optimization; electromagnetic field exposure; geospatial optimization

Check for updates

Academic Editor: Yan (Rockee) Zhang

Received: 13 May 2026
Revised: 31 July 2026
Accepted: 19 August 2026
Published: 28 August 2026

Copyright: © 2026 by the authors. Licensee MDPI, Basel, Switzerland. This article is an open access article distributed under the terms and conditions of the Creative Commons Attribution (CC BY) license.

1. Introduction

As the use of Unmanned Aerial Vehicles (UAVs), commonly referred to as drones, becomes increasingly widespread across numerous civilian sectors, in addition to military applications, the necessity of a comprehensive framework of regulations and technologies capable of facing this rapid development is also growing. In particular, the aviation sector is currently focusing on the development of innovative Communication, Navigation, and Surveillance (CNS) infrastructures, but also networks designed to support the emerging needs of Urban and Advanced Air Mobility (UAM/AAM).

The design of ground-sensor networks for AAM surveillance, more specifically for U-Space surveillance services in Europe [1–3], has progressively evolved from generic facility-location formulations toward mission-driven deployment strategies that explicitly

incorporate detection physics and operational constraints. Even though formal surveillance-performance requirements for UAM and U-space operations are still evolving, established frameworks for ground-based surveillance systems provide useful reference criteria for deployment planning. In particular, ref. [4] defines performance concepts related to surveillance coverage and detection capability, which have also been adapted to emerging UAM applications in recent studies. In this work, these concepts are not used as certification requirements but rather as a reference context for the development of a deployment-oriented planning framework.

In the literature, among AAM-specific approaches, the Surveillance for AAM Network Design (SAND) model formulates sensor placement as a binary integer optimization problem, enforcing a minimum detection probability and full-coverage constraints, while simultaneously minimizing deployment cost [5]. In parallel, the broader radar placement literature has matured toward multi-objective optimization problems, balancing coverage performance against resource constraints such as the number of sensors and deployment costs. In particular, recent studies have investigated adaptive meta-heuristic algorithms for radar network optimization, establishing robust Pareto-optimal baselines that can also serve as benchmarks for evaluating simpler greedy or heuristic strategies [6].

In operational environments where topography, buildings, and obstacles play a significant role, such as port basins or urban aprons, terrain-aware sensor deployment studies have shown that "effective coverage" must be evaluated across multiple altitude layers. These altitude-dependent assessments are then aggregated into a unified optimization objective in order to accurately reflect overall surveillance performance. This perspective has been adopted, for instance, when assigning higher weights to low-altitude corridors and regions surrounding vertiports and heliports, ensuring that critical operational zones receive prioritized coverage [7].

A complementary line of research moves beyond the traditional binary in/out coverage paradigm by modelling radar performance as a continuous surrogate sensing field. In this perspective, Frequency Modulated Continuous Wave (FMCW) radar coverage is represented as a smooth function of range and angular characteristics, allowing sensor deployment to be optimized directly with respect to a continuous surrogate sensing model rather than binary visibility constraints [8]. This approach naturally motivates the use of Gaussian surrogate sensing kernels, which provide a compact and physically interpretable representation of spatial sensing effectiveness and can be readily parameterized to reflect realistic radar characteristics. Similar kernel-based formulations are also supported by recent probabilistic sensor placement methods that learn spatially varying coverage models from data when site-specific information is available [9].

Another fundamental aspect to consider is the role of relative sensor-target geometry in determining detection performance for non-cooperative UAS. In bistatic radar formulations, detection probability is commonly expressed as a function of the relative positions and orientations of transmitter, receiver, and target, jointly accounting for target RCS, propagation losses, as well as occlusion effects. These models provide a closed-form or semi-analytical relationship that explicitly links geometric configuration to detection likelihood along plausible approach trajectories [10]. This dependence on geometry extends beyond single-sensor performance and becomes a network-level property in distributed detection systems. In such settings, unfavorable alignments or near-collinear sensor layouts can lead to poor observability even in nominally covered regions. In [11], sensor and antenna placement is formulated as a sequential decision-making problem and addressed using reinforcement-learning-based strategies, with the objective of preserving effective coverage under dynamically varying target headings and trajectories. This perspective directly motivates spatially structured planning approaches in which coverage objectives

are modulated by expected motion patterns. In particular, it naturally complements the use of interest-weighted route segments, where detection resources are preferentially allocated along flight corridors and approach paths that are both operationally critical and geometrically sensitive.

Recent studies on UAM route localization, in particular a recent NASA investigation [12], have shown that achievable meter-level localization accuracy is primarily governed by ground-sensor geometry, rather than by target-dependent characteristics alone. In particular, the relative placement of ground nodes, the resulting intersection angles, and field-of-view constraints directly determine the observability of the vehicle state along nominal flight corridors. In practical terms, these findings highlight the presence of geometry-limited segments, both near take-off and landing zones and along segments where sensor alignment leads to poor intersection geometry. In such conditions, coverage-based planning should be supported by a separate geometric analysis. In the current implementation, the polygonal feasibility layers are defined by the user and can incorporate geometry-based siting constraints derived externally. The optimizer does not itself estimate localization accuracy, intersection angles, or field-of-view observability.

From a hardware feasibility standpoint, recent demonstrations of compact FMCW radar nodes operating at low effective isotropically radiated power (EIRP) in the 24–77 GHz frequency range support the practical relevance of this modelling approach. The proposed framework is hardware-agnostic and is designed to represent a general class of short-range radar systems through abstract detection parameters. Fully integrated 24 GHz transceivers, hybrid-beamforming CMOS radars for small-UAS detection, and automotive 77 GHz radars adapted for UAS altimetry collectively demonstrate that short-range detection can be achieved with small apertures, moderate beamwidths, and conservative CFAR thresholds [13–15].

In parallel, electromagnetic exposure is modelled through a co-registered power-density layer expressed in W/m^2 and derived from EIRP and propagation distance. ITU-T Recommendation K.91 [16] provides a reference context for subsequent exposure assessment, while ETSI GR ISC 001 [17] describes representative use cases and deployment scenarios for integrated sensing and communications systems. In the present implementation, no regulatory exposure limit is embedded in siting or optimization; the computed layer is a first-order screening output that may be compared with applicable limits in a separate, site-specific assessment.

Overall, the proposed formulation combines user-defined siting feasibility, normalized surrogate sensing-score planning, and post-processing exposure screening. It does not directly model geometric observability or verify regulatory compliance. Related studies in airport and seaport environments illustrate operational contexts characterized by spatially localized surveillance tasks, constrained infrastructure, and heterogeneous monitoring priorities [18–21]. These works are cited as representative application-context studies rather than as direct contributions to radar-site optimization.

The main contributions of this work can be summarized as follows:

- A geospatial decision-support framework for radar deployment under explicit siting constraints;
- A deployment-oriented surrogate sensing model for continuous normalized detection-score evaluation;
- An interest-weighted optimization strategy for prioritizing critical surveillance regions;
- A first-order electromagnetic exposure-screening layer for early-stage scenario comparison;
- An operator-oriented implementation for realistic AAM scenarios.

2. Motivation

Ensuring continuous surveillance of non-cooperative drones is a central challenge for safety authorities and critical-infrastructure operators. Indeed, one of the main problems is that small UAVs exhibit low radar cross-sections (RCS), irregular flight paths, and intermittent visibility, often leading to missed detections when using single-sensor systems [22]. Moreover, especially in urban scenarios, environmental clutter, occlusions, and the absence of cooperative signals further reduce reliability. These limitations motivate the need for distributed ground-sensor networks capable of maintaining persistent coverage through geometric diversity and redundancy.

Therefore, as discussed in the previous section, low-power FMCW radars, which can operate continuously, day and night, and under adverse weather, represent a viable solution for short-range surveillance [13–15].

However, such deployments must balance three competing objectives:

- Maximize detection reliability in high-interest zones (e.g., approach corridors, quay lines, or energy facilities).
- Respect siting constraints defined by accessibility, ownership, and safety limits.
- Compute first-order electromagnetic exposure indicators under the adopted low-EIRP assumptions.

The proposed system explicitly couples these elements into a single, deterministic planning workflow. By optimizing radar siting on a geospatially constrained grid and visualizing both detection score and power density, operators can support deployment decisions, compare trade-offs, and perform preliminary exposure screening before physical installation; formal compliance assessment remains outside the current implementation.

3. System Description

The developed system is an operator-facing planning tool designed for low-power radar surveillance in dense, operationally constrained environments such as airports and seaports. Users define feasible installation zones (cyan polygons) and high-priority surveillance areas (magenta polygons) directly on a satellite basemap, as shown in Figure 1. These areas are discretized onto a computational grid, where eligible cells represent admissible installation sites and weighted cells encode surveillance priority.

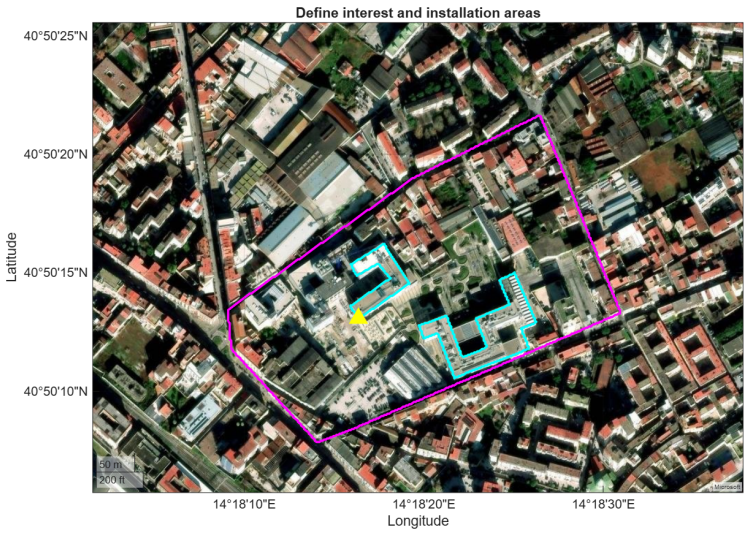

Figure 1. Example of the definition of installation zones (cyan polygons) and high-priority surveillance areas (magenta polygons). The yellow triangle represents the sensor.

Each radar is modelled through a truncated Gaussian surrogate sensing kernel, and the contributions of multiple radars are combined to form a cumulative detection-score field over the area of interest. Based on a predefined radar budget, K, the system determines a suitable deployment configuration within the feasible regions, accounting for diminishing returns in already covered areas.

The tool produces two co-registered outputs:

- A detection score map, highlighting effective coverage areas.
- A power-density map (in $/m^2$), derived from radar EIRP and distance, displayed with a fixed colour scale to ensure comparability.

To maintain computational efficiency, the implementation supports grids of up to 400×400 cells and interactive execution on standard hardware. Moreover, for the current application, the framework was implemented in MATLAB R2026a using the Mapping Toolbox, Image Processing Toolbox, and Statistics and Machine Learning Toolbox, and was executed on a computer equipped with an Intel Core i7-1380P processor and 32 GB of RAM, running Windows 11 Pro.

Architecture and Processing Pipeline

The architecture of the proposed framework is shown in Figure 2. The system is organized as a sequential processing pipeline that links geospatial input definition, surrogate sensing modelling, radar placement optimization, exposure evaluation, and output generation.

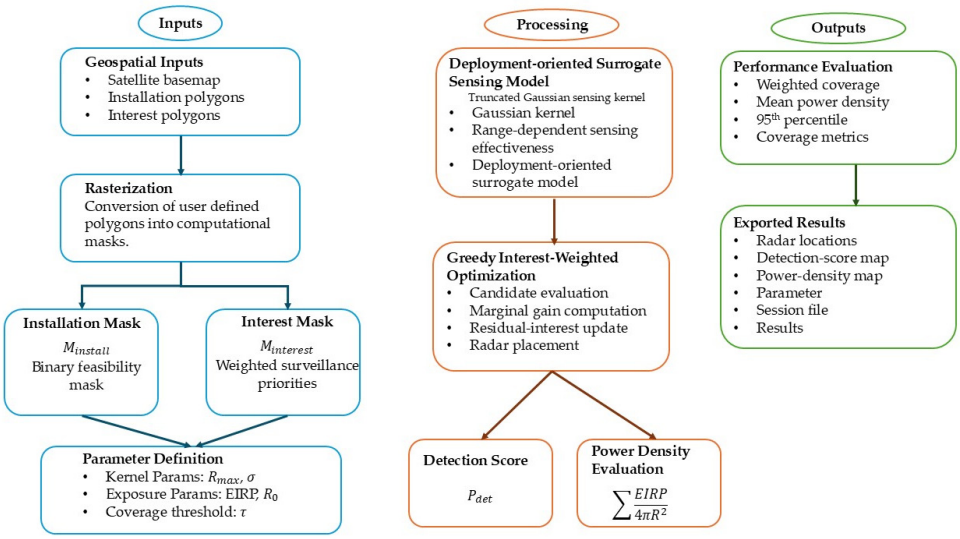

Figure 2. System architecture and processing pipeline of the proposed radar-deployment framework. User-defined geospatial inputs are rasterized into an installation mask and an interest-weight map, combined with planning, sensing, and exposure parameters, and processed through the surrogate sensing model and greedy optimization procedure. The selected radar locations are then used to generate the sensing-score and power-density maps, from which performance indicators and exported results are derived.

The first stage concerns the definition of the geospatial inputs. Feasible radar installation areas and surveillance regions of interest are specified by the user as polygons over a satellite basemap. These polygons are rasterized onto a georeferenced computational grid, producing two spatial layers. The first layer is the binary installation mask, $M_{install}$, which identifies the grid cells where radar deployment is admissible. The second layer is the interest mask, $M_{interest}$, which identifies the surveillance region considered by the optimization. A derived non-negative priority map, $M_{weighted}$, is subsequently obtained by modulating the interest mask according to the ground distance from installation/building regions.

In addition to the geospatial layers, the framework requires a set of numerical parameters. These include the radar budget K, the maximum sensing range R_{max}, the Gaussian kernel width σ, EIRP, the near-field distance clamp R_0, and the coverage threshold τ. These parameters define the surrogate sensing model, the exposure-screening model, and the criteria used for performance assessment. In the current GUI, K, EIRP, R_0, and τ are editable; the baseline implementation fixes $R_{max} = 250$ m and derives $\sigma = R_{max}/2.5 = 100$ m.

The processing stage begins with the construction of a surrogate sensing model. In this model, each radar is represented by a truncated Gaussian surrogate sensing kernel that provides a range-dependent approximation of detection effectiveness. The kernel is used as a deployment-oriented surrogate and is not intended to reproduce the full radar detection chain or a calibrated probability-of-detection model.

Radar placement is then performed through a greedy interest-weighted optimization procedure. At each iteration, candidate radar locations are evaluated within the admissible installation mask, and the location providing the largest marginal increase in the residual interest-weighted detection score is selected. After each placement, the residual interest is updated in order to reduce the priority of regions that have already been covered and to favor subsequent placements in still under-covered areas.

Once the radar locations have been selected, the framework generates two spatial output layers. The cumulative sensing-score map, P_{det}, is obtained by fusing the contributions of the selected radar kernels using an independent-union formulation. In parallel, the electromagnetic exposure layer is computed as a co-registered power-density map, S, using the selected radar locations, the assigned EIRP values, and the near-field distance clamp R_0. This layer is used as an exposure-screening output and is not involved in the radar-placement optimization. The detailed power-density formulation is provided in Section 5.4.

The final stage consists of performance evaluation and result export. The selected radar locations, the cumulative sensing-score map, the power-density map, the configuration parameters, and the corresponding performance metrics are stored for subsequent analysis and comparison across deployment scenarios. The reported performance indicators include weighted coverage, mean power density, and the 95th-percentile power density. The correspondence between the main processing stages and their outputs is summarized in Table 1.

Table 1. Main processing stages, inputs, operations, and outputs of the proposed planning framework.

Stage	Main Inputs	Operation	Outputs
Geospatial definition	Satellite basemap, user polygons	Interactive drawing of interest and installation areas	Polygon layers
Rasterization	Polygon layers, map limits, grid size	Conversion to grid-based masks	$M_{interest}$, $M_{install}$
Parameter setting	K, EIRP , R_0, τ; fixed R_{max} and σ in the baseline	Definition of sensing and exposure parameters	Model configuration
Kernel generation	Grid spacing, R_{max}, σ	Generation of truncated Gaussian surrogate sensing kernel	Sensing kernel
Greedy placement	$M_{weighted}$, $M_{install}$, kernel, K	Iterative selection of radar sites	Radar deployment mask
Interest weighting	$M_{interest}$, $M_{install}$, Δx, Δy, d_{buffer}, w_{min}	Anisotropic distance transform and exponential priority weighting	$M_{weighted}$
Score fusion	Radar sites, kernel	Independent-union accumulation of sensing score	P_{det} map

Table 1. *Cont.*

Stage	Main Inputs	Operation	Outputs
EMF screening	Radar sites, EIRP, R_0	Free-space power-density computation	S map
Evaluation/export	P_{det} , S, selected sites	Computation of metrics and file export	Tables, maps, session bundle

4. Reference Radar Models

To motivate the representative sensing assumptions adopted throughout the proposed deployment-planning framework, two reference systems are considered (Table 2): a low-power Software Defined Radio (SDR)-based FMCW radar built on the Analog Devices ADALM-PLUTO platform (RF front-end: AD9363) [23], adopted as a representative ground radar node, and the DJI Mavic 3 Multispectral (Mavic 3M) (DJI, Shenzhen, China) [24], used as a representative small-UAS target. These systems are not used as operational radar implementations within the framework; rather, they provide representative reference platforms for the surrogate-model assumptions.

Table 2. Hardware specifications.

Category	Parameter	Value/Range	Physical Meaning
Radar Core	RF Transceiver	AD9363 (1T1R) Integrated SDR platform	Integrated SDR platform
	Frequency Range	325–3800 MHz	ISM/sub-6 GHz operation
	Channel Bandwidth	$\leq$20 MHz	Determines range resolution
Target	Platform	DJI Mavic 3M	Sub-1 kg multirotor class
	Mass	951 g	With RTK module
	Dimensions	347.5 × 283 × 139.6 mm	Open, no propellers
	Max Speed	15 m/s	Kinematic envelope
	Max Flight Time (no wind)	Up to 43 min	Endurance under still-air conditions.
Reflectivity	Typical RCS	−8 to −19 dBsm	Aspect-dependent
	RCS @ X-Band	−15 to −20 dBsm	Conservative estimate

The proposed planner is hardware-agnostic. The Pluto/AD9363 platform is employed solely as a representative low-power SDR reference, while the surrogate sensing model is parameterized through representative sensing assumptions rather than hardware-specific performance metrics or radar-equation calibration.

This abstraction allows the proposed framework to be applied to different classes of short-range systems without modifying the underlying optimization methodology.

The selected reference systems satisfy the typical requirements of urban and semi-urban surveillance deployments, namely:

- strict low-emission radar power budgets to ensure safety and electromagnetic coexistence;
- compact size, low power consumption, and reduced cost, enabling dense siting on existing infrastructure;
- availability of well-documented platform kinematics and RF characteristics for defining representative planning assumptions.

Regarding the radar node, the ADALM-PLUTO/AD9363 platform is considered as a representative low-power SDR reference. Its tuning range, approximately 325–3800 MHz,

and channel bandwidth up to 20 MHz provide a documented example of a compact radar-capable platform suitable for prototyping a low-EIRP sensing concept [23]. However, the proposed framework is not tied to this specific RF front-end. Antenna characteristics, carrier frequency, and receiver-chain parameters are not explicitly modelled in the optimizer; their effects are represented only indirectly through the surrogate sensing assumptions introduced in Section 4.

The DJI Mavic 3 Multispectral is used as a representative small-UAS target because of its documented dimensions, mass, endurance, and operational characteristics [24]. These parameters provide a realistic target context for deployment planning, without implying that the proposed model is calibrated to a specific target aspect or flight condition.

Small-UAS RCS is known to vary significantly with frequency, aspect angle, material composition, and rotor-induced micro-Doppler effects. Literature values reported around 24 GHz and in X-band indicate RCS ranges on the order of -8 to -19 dBsm and -15 to -20 dBsm, respectively, depending on platform and measurement conditions [25–27]. These RCS values are reported solely to characterize the variability of the representative target class. They are not used to derive $R_{\max}$, σ, or a calibrated probability of detection for the proposed surrogate sensing model.

Overall, the objective of the reference-system discussion is not to characterize a specific radar implementation, but to provide physically plausible assumptions for the deployment-planning framework. The sensing-kernel parameters are therefore selected as representative planning assumptions and are further assessed through the sensitivity analysis reported in Section 7.

The proposed framework is designed as a high-level deployment-planning tool rather than as a radar signal-processing or detection pipeline. It does not process raw FMCW samples, implement a complete radar equation, or derive a calibrated normalized detection score from a specific radar configuration. Instead, radar performance is represented through a normalized, surrogate sensing model that captures the expected spatial decay of detection effectiveness.

Within this formulation, the Gaussian kernel provides a deployment-oriented approximation of the sensing footprint. The parameters R_{max} and σ define the spatial support and decay of the detection score, while $p_0 = 1$ denotes the normalized peak score at the radar location. The EIRP parameter is used only for power-density evaluation and does not calibrate the sensing-score map.

5. Radar Installation Optimization Algorithm

5.1. Graphical User Interface Overview

The graphical user interface (GUI) implemented in MATLAB provides an intuitive environment for planning radar deployments directly on a geospatial basemap. An example of the interface is shown in Figure 3. The GUI combines a satellite-basemap panel, used for the interactive definition of surveillance and installation areas, with a parameter-control panel used to specify the main planning, sensing, and exposure parameters.

The interface follows a two-stage workflow aligned with the operator planning process.

In the first stage, users define the problem geometry by drawing magenta polygons for surveillance zones and cyan polygons for feasible installation areas. The polygons are rasterized onto the fixed analysis grid and remain editable during the current session. Any subsequent modification of their vertices automatically updates the corresponding spatial masks before optimization.

In the second stage, the user specifies the number of radars K, EIRP, the near-field clamp R_0, and the coverage threshold τ. The framework then executes the greedy interest-weighted optimization, computes the cumulative sensing-score field, and identifies the

selected radar locations. The resulting sensing-score and power-density maps are displayed as georeferenced overlays on the basemap to support visual comparison of alternative deployment scenarios.

The corresponding configuration parameters, selected radar locations, output maps, and performance metrics are stored for subsequent analysis and comparison.

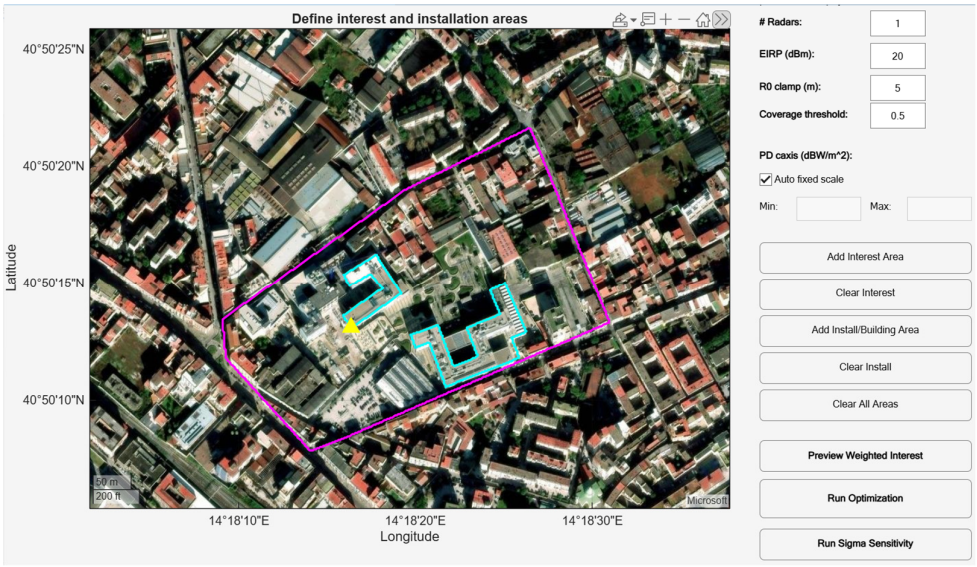

Figure 3. Example of the MATLAB graphical user interface used to define geospatial planning inputs and numerical parameters before radar-placement optimization.

5.2. Optimization Formulation

The radar installation optimizer determines where to place a limited number K of low-power ground radars in order to maximize the total interest-weighted coverage of the surveillance area. In other words, the algorithm does not maximize the minimum detection score over all grid cells; rather, the objective is expressed in the discrete form:

$$J = \sum_{u \in \Omega} w_u P_{det}(u), \tag{1}$$

where Ω denotes the set of grid cells in the analysis domain, w_u is the interest weight associated with cell u and $P_{det}(u)$ is the normalized detection score produced by the surrogate sensing model. This formulation favors configurations that allocate sensing resources where surveillance is most valuable, rather than enforcing uniform coverage over the entire area.

5.3. Grid Representation and Mask

The surveillance area is discretized into a georeferenced computational grid aligned with the basemap. Each grid cell is identified by the index pair $u = (i, j)$, with $i = 1, \ldots, N_{row}$ and $j = 1, \ldots, N_{col}$. The geographical extent of the analysis is fixed throughout a saved session and is stored independently of the current map viewport. The corresponding east–west and north–south grid spacings are denoted by Δx and Δy, respectively.

The adopted representation is two-dimensional and describes the ground-projected surveillance area. This assumption is consistent with the deployment-planning scope of the framework, which focuses on the placement of ground-based sensors under geographical and operational constraints. Altitude-dependent sensing models and full three-dimensional surveillance-volume optimization are left for future work.

Two primary raster layers are associated with the grid. The first is an interest weight $w_u \geq 0$, obtained by rasterizing the operator-defined interest polygons into the matrix $M_{interest} \in R^{N_{row} x N_{col}}$; higher values correspond to higher surveillance priority. In the reported experiments, the rasterized interest layer is converted into a non-negative weighted priority map. Weights are assigned only within the user-defined surveillance-priority regions and are reduced inside or near installation/building areas according to their distance from the installation mask; the resulting map is then normalized to the range [0, 1].

More specifically, let d_{ij} denote the anisotropic Euclidean ground distance between grid cell (i, j) and the nearest cell belonging to the installation mask. The distance-dependent weighting factor is defined as

$$w_{ij} = w_{min} + (1 - w_{min})[1 - \exp(-\frac{d_{ij}}{d_{buffer}})] \quad (2)$$

where $w_{min} = 0.10$ is the minimum retained interest factor and $d_{buffer} = 80\,\mathrm{m}$ is the exponential transition distance. For cells belonging to the installation mask, $w_{ij} = w_{\min}$. The unnormalized weighted-interest map is then obtained as:

$$\widetilde{M}_{\mathrm{weighted}}(\mathrm{i},\mathrm{j}) = \begin{cases} M_{\mathrm{interest}}(\mathrm{i},\mathrm{j})\, w_{ij}, & M_{\mathrm{interest}}(i,j) > 0, \\ 0, & \text{otherwise.} \end{cases} \quad (3)$$

Finally, provided that its maximum value is positive, the map is normalized according to

$$M_{weighted}(i,j) = \frac{\widetilde{M}_{weighted}(i,j)}{max_{p,q}\widetilde{M}_{weighted}(p,q)}, \quad (4)$$

and the resulting values are constrained to the interval $[0,\ 1]$.

The second attribute is a feasibility mask $m_c \in \{0,1\}$, derived from the installation polygons and stored in $M_{install}$, which indicates whether a radar can physically be deployed (e.g., rooftops, mast tops, etc.).

The set of admissible radar locations is therefore defined as:

$$\mathcal{C} = \{c\ : m_c = 1\}, \quad (5)$$

These definitions are independent of the specific radar model and are valid for any deployment scenario considered within the proposed framework. Given a radar budget K, the optimization problem consists of selecting up to K radar locations from $\mathcal{C}$ and computing the corresponding cumulative sensing-score field over the grid.

5.3.1. Gaussian Surrogate Sensing Kernel

While the grid representation and masking strategy described above are scenario-driven, the following step introduces the parametrized surrogate sensing model used by the optimizer. Consistently with the modelling assumptions discussed in Section 4, each radar is represented by a truncated Gaussian surrogate sensing kernel defined on the georeferenced computational grid. Similar continuous coverage formulations have been used in radar-network deployment studies, where radar coverage is represented through spatially varying coverage-strength functions rather than through a complete signal-processing chain [8].

For a radar located at a candidate radar location $c = (i_c, j_c)$ and a grid cell $u = (i, j)$, the ground metric distance used by the kernel is:

$$D_c(u) = \sqrt{[(j - j_c)\Delta x]^2 + [(i - i_c)\Delta y]^2} \quad (6)$$

The finite kernel support is circular in the adopted local ground-metric representation, up to the spatial discretization of the grid. In the baseline configuration, R_{max} = 250 m, p_0 = 1, and $\sigma = R_{max}/2.5$ = 100 m.

With this choice, the untruncated Gaussian value at $R_{\max}$ is approximately $e^{(-3.125)} \approx 0.044$, so the kernel is truncated where its residual contribution is already small. This choice provides a smooth range-dependent decay while maintaining a compact computational footprint. The sensitivity of the results to σ is analysed in Section 7.

The main parameters adopted in the baseline configuration are summarized in Table 3. The table distinguishes between parameters used to define the surrogate sensing kernel, parameters used for the exposure-screening layer, and parameters used only for performance evaluation.

Table 3. Baseline parameters adopted for the surrogate sensing kernel, exposure-screening layer, and performance evaluation.

Parameter	Value	Role in the Framework
R_{max}	250 m	Maximum effective sensing range
σ	100 m	Controls range-dependent score decay
p_0	1	Normalized peak detection score
EIRP	20 dBm	Power-density evaluation parameter
R_0	5 m	Near-field clamp for exposure calculation
τ	0.5	Coverage threshold
d_{min}	60 m	Minimum radar-site spacing in the raster-distance approximation
d_{buffer}	80 m	Exponential transition distance around installation/building regions
w_{min}	0.10	Minimum retained interest factor inside installation/building regions

It should be noted that EIRP and R_0 are not used to calibrate the detection-score map; they are used only for the electromagnetic exposure layer. Similarly, τ is applied only during the evaluation of weighted coverage and does not affect the radar-placement optimization.

5.3.2. Greedy Placement with Residual Interest

Radar sites are selected using a greedy, interest-weighted coverage heuristic. The algorithm maintains a cumulative sensing-score field $P_{det}(u)$, initially set to zero over the grid, and a residual interest map $R(u)$, initialized as $R(u) = w_u$. A binary deployment mask M_{radars} is also maintained to mark the locations of the selected radar sites.

At each iteration $r = 1, \ldots, K$, all admissible locations $c \in \mathcal{C}$ are evaluated by aligning the Gaussian kernel with the grid and computing the marginal gain:

$$\Delta J(c) = \sum_{u \in \mathcal{N}(c)} R(u)\, k_c(u), \tag{7}$$

where $\mathcal{N}(c)$ denotes the set of grid cells covered by the kernel centered at c, and $k_c(u)$ is the corresponding kernel value at cell u. When the kernel footprint intersects the boundary of the computational domain, $\mathcal{N}(c)$ is restricted to the valid grid cells inside the rasterized analysis area. The quantity calculated in (7) measures how much residual interest would be covered by installing a radar at c.

The location c^* with the highest marginal gain $\Delta J(c)$ is selected as the next radar site. In the case of equal marginal-gain values, the first candidate encountered in the fixed order returned by the installation-mask scan is retained. Following this selection, both the

cumulative sensing-score field and the residual interest map are updated over the kernel footprint $\mathcal{N}(c^*)$ according to:

$$P_{det}(u) \leftarrow 1 - (1 - P_{det}(u))(1 - k_{c^*}(u)), \ \ u \in \mathcal{N}(c^*) \tag{8a}$$

$$R(u) \leftarrow R(u)(1 - k_{c*}(u)), \ \ u \in \mathcal{N}(c^*) \tag{8b}$$

This update mechanism progressively suppresses residual interest in regions that are already well covered, while preserving higher weights in partially covered or uncovered areas. As a result, subsequent radar placements are naturally guided toward still-uncovered, high-priority regions, discouraging unnecessary clustering of sensors.

The iterative process terminates when the radar budget K is exhausted or when no admissible location yields a positive marginal gain.

In compact form, the algorithm implements the discrete interest-weighted objective introduced in Equation (1).

In the proposed implementation, the weighting term is not uniform across the area of interest. Cells located inside or in close proximity to installation regions are assigned lower weights, while higher weights are assigned to the surrounding operational areas. This weighting strategy reflects the objective of prioritizing surveillance effectiveness in the portions of the environment where unauthorized UAV activity is more operationally relevant.

The adopted greedy strategy is heuristic in nature and therefore does not guarantee global optimality. It was selected to ensure computational efficiency and interactive execution on large geospatial grids.

5.4. Power Density Evaluation

Once the radar sites have been selected by the optimization procedure, the tool evaluates the electromagnetic exposure associated with the deployed configuration by computing a spatial power-density field over the analysis grid. This evaluation is not used to drive the placement algorithm in the present implementation, but it provides a co-registered first-order exposure-screening map for scenario comparison at the planning stage.

Each radar is characterized by its EIRP, expressed in watts. Within the localized exposure-screening model implemented in the code, the contribution of a radar at distance d is evaluated with the free-space expression only for $d \leq R_{max}$:

$$S(d) = \frac{EIRP}{4\pi d^2}, \qquad d \leq R_{max} \tag{9}$$

The contribution is set to zero for $d > R_{max}$. The effective distance $d_{eff} = max(d, R_0)$ is used inside the modeled range.

Here d denotes the ground distance between a radar and a grid cell, evaluated with separate local meters-per-degree factors in longitude and latitude. Increasing EIRP increases the computed values within R_{max}, while selected radar locations determine their spatial distribution. This is a localized, first-order screening approximation and does not account for antenna patterns, beam shaping, environmental attenuation, or detailed near-field propagation.

The total power density at each grid cell is obtained by summing the contributions of all deployed radars. Radar locations, originally expressed in geographic coordinates, are mapped onto the local metric grid using standard meters-per-degree approximations consistent with the basemap projection.

The power-density field is stored in W/m^2 and converted to dBW/m^2 for visualization. With automatic scaling, a common color scale is used for radar-budget comparisons performed with the same EIRP, R_0, and R_{max} values. Scenarios with different emission parameters require an explicitly shared manual scale for direct visual comparison.

Although power density is currently used as an evaluation and visualization layer, the same formulation naturally supports extensions in which exposure constraints are enforced explicitly, for instance by excluding candidate sites that would violate regulatory limits in sensitive areas or by penalizing high-exposure configurations in extended optimization runs.

5.5. Outputs and Derived Performance Metrics

The optimization process yields a binary deployment mask M_{radars}, the corresponding set of selected radar sites expressed as grid indices and georeferenced coordinates, a cumulative detection-score map $P_{det}(u)$, and a power-density map $S(u)$. These outputs provide a complete spatial description of the surveillance performance and the associated electromagnetic exposure for a given deployment configuration.

From these fields, a set of aggregate performance indicators is derived to support quantitative evaluation and comparison across scenarios. In particular, interest-weighted coverage metrics are computed by evaluating the fraction of the total surveillance priority mass located in grid cells where the cumulative detection score exceeds a predefined design threshold. In parallel, exposure-related indicators are extracted from the power-density field, including spatial averages and high-percentile values.

These indicators are used exclusively for performance assessment and reporting and do not directly influence the placement decisions in the current implementation. Their role is to enable transparent comparison between different radar budgets, kernel parameterizations, and deployment scenarios, as illustrated in the Results section.

6. Experimental Scenario

Figures 4–6 illustrate an example set of input masks and the corresponding detection score and power-density maps produced by the optimizer under nominal parameters. To evaluate the performance of the proposed planning framework, simulations were conducted on the San Giovanni a Teduccio campus (Naples, Italy), a representative semi-urban scenario characterized by buildings, open courtyards, and heterogeneous surveillance priorities. The study area extends approximately 1.0 × 0.8 km and is represented on a 400 × 400 georeferenced computational grid.

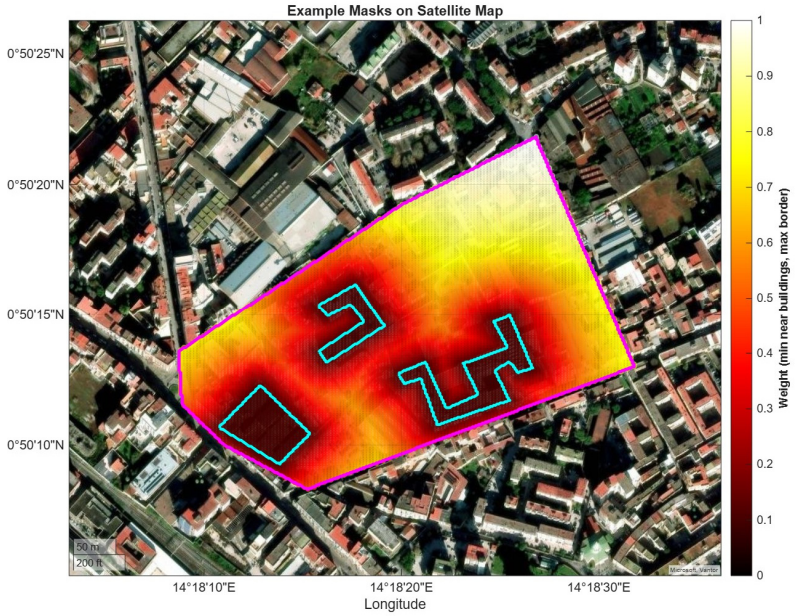

Figure 4. Input interest-weighted surveillance mask and feasible radar installation regions for the AAM case study.

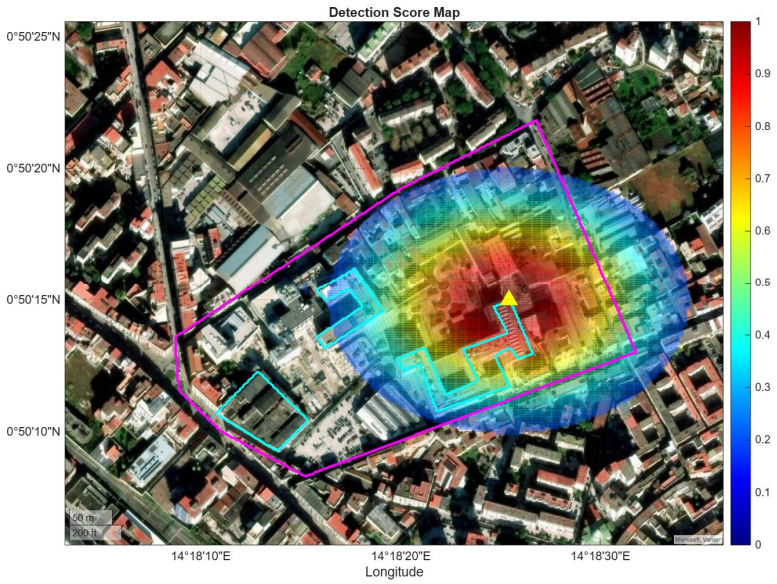

Figure 5. Detection-score map resulting from interest-weighted optimization for a single-radar ($K = 1$) deployment.

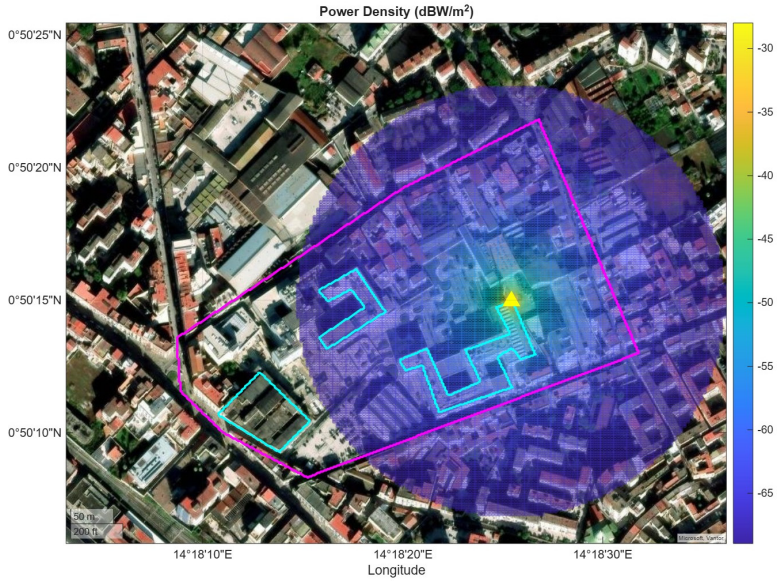

Figure 6. Power-density distribution associated with the optimized single-radar ($K = 1$) deployment.

Figure 4 shows the input interest-weighted surveillance mask and feasible radar installation regions for the AAM case study. White and yellow tones denote higher weights, whereas orange, red, and darker tones represent progressively lower weights. The magenta contour identifies the interest region, and cyan contours identify cells in which radar installation is admissible.

The semi-transparent overlay of the interest and installation masks on the satellite basemap provides a direct visual representation of the operational environment and planning objectives, while preserving visibility of underlying terrain features such as buildings and open spaces. Together, these layers define the inputs to the optimization algorithm, which seeks to maximize interest-weighted coverage under explicit installation constraints.

Figure 5 presents the detection-score map obtained after optimization for the single-radar configuration. The radar is deployed within one of the feasible installation regions and provides coverage over the surrounding open areas of the campus. The interest-weighted planning strategy assigns lower priority to the interior of the installation buildings

and higher priority to the surrounding operational areas, leading the optimizer to favor configurations that maximize sensing effectiveness over the most relevant portions of the surveillance region. The resulting coverage field illustrates the gradual decrease in sensing effectiveness with distance from the radar location, as represented by the adopted Gaussian surrogate model. Figure 6 presents the corresponding power-density map for the single-radar configuration. As expected from the adopted free-space propagation model, the highest power-density levels are concentrated in the immediate vicinity of the installation site and decrease progressively with distance. The resulting exposure field remains spatially localized around the radar location, while the majority of the monitored area is characterized by substantially lower power-density levels.

Together, Figures 5 and 6 illustrate how the proposed framework simultaneously accounts for installation feasibility, interest-weighted coverage objectives, and electromagnetic-exposure assessment within a realistic AAM surveillance scenario.

On the reference computer described in Section 3, a complete optimization run required approximately 2 to 8 s, depending on the selected radar budget.

7. Results

Each radar was modelled using the truncated Gaussian surrogate sensing kernel introduced in Section 5.3.1, with $R_{max} = 250$ m, $\sigma = 100$ m, and normalized peak detection score $p_0 = 1$. The EIRP was set to 20 dBm (0.1 W) per node and was used only for the power-density exposure-screening layer.

Simulations were performed for radar budgets $K = 1$ to 10, with each configuration evaluated independently. This analysis enables a systematic assessment of how surveillance performance and exposure levels scale with the number of deployed radar nodes.

7.1. Coverage Performance and Exposure Analysis

Table 4 summarizes the quantitative performance of the proposed deployment strategy as a function of radar budget K.

The interest-weighted coverage metric represents the fraction of the weighted surveillance-priority map achieving a detection score above the selected design threshold. The weighting scheme assigns lower priority to installation and building regions, while progressively increasing the importance of the surrounding operational areas. This choice reflects the objective of maximizing surveillance effectiveness in the portions of the environment where unauthorized UAV activity is most relevant, rather than within the installation sites themselves.

Exposure statistics are computed over the full analysis grid and include the mean and 95th-percentile power-density values, reported in $\mu W/m^2$. These indicators are intended to support comparison between deployment configurations and to provide an early-stage assessment of the spatial distribution of electromagnetic exposure.

Table 4. Summary of coverage and exposure metrics for different radar budgets.

Number of Radars (K)	Weighted Coverage (%)	Mean Power Density ($\mu W/m^2$)	95th Percentile ($\mu W/m^2$)
1	30.308	0.447	1.013
3	78.920	1.342	3.908
6	93.034	2.683	9.745
9 (10 requested)	94.783	4.013	17.293

Moreover, it is worth noting that, although the optimization was also performed with a requested radar budget of $K = 10$, the algorithm was unable to deploy all ten radar

sites because the available installation areas did not provide enough feasible locations while satisfying the minimum inter-radar spacing constraint. Depending on the value of the kernel standard deviation σ, only eight or nine radar sites could be placed before the optimization terminated. In particular, Table 4 reports the results for the case of $\sigma = 100$ m, which allows the deployment of nine radars, rather than the requested configuration with $K = 10$.

Figure 7 presents the detection-score maps and the corresponding power-density distributions for increasing radar budgets. As expected, increasing the number of deployed radars improves the spatial extent of effective coverage through overlapping detection regions, while also increasing the cumulative power-density levels around the installation sites. As mentioned before, for $K = 10$, only nine of the 10 requested radars were placed, because no remaining candidate site satisfies the minimum spacing of 60 m.

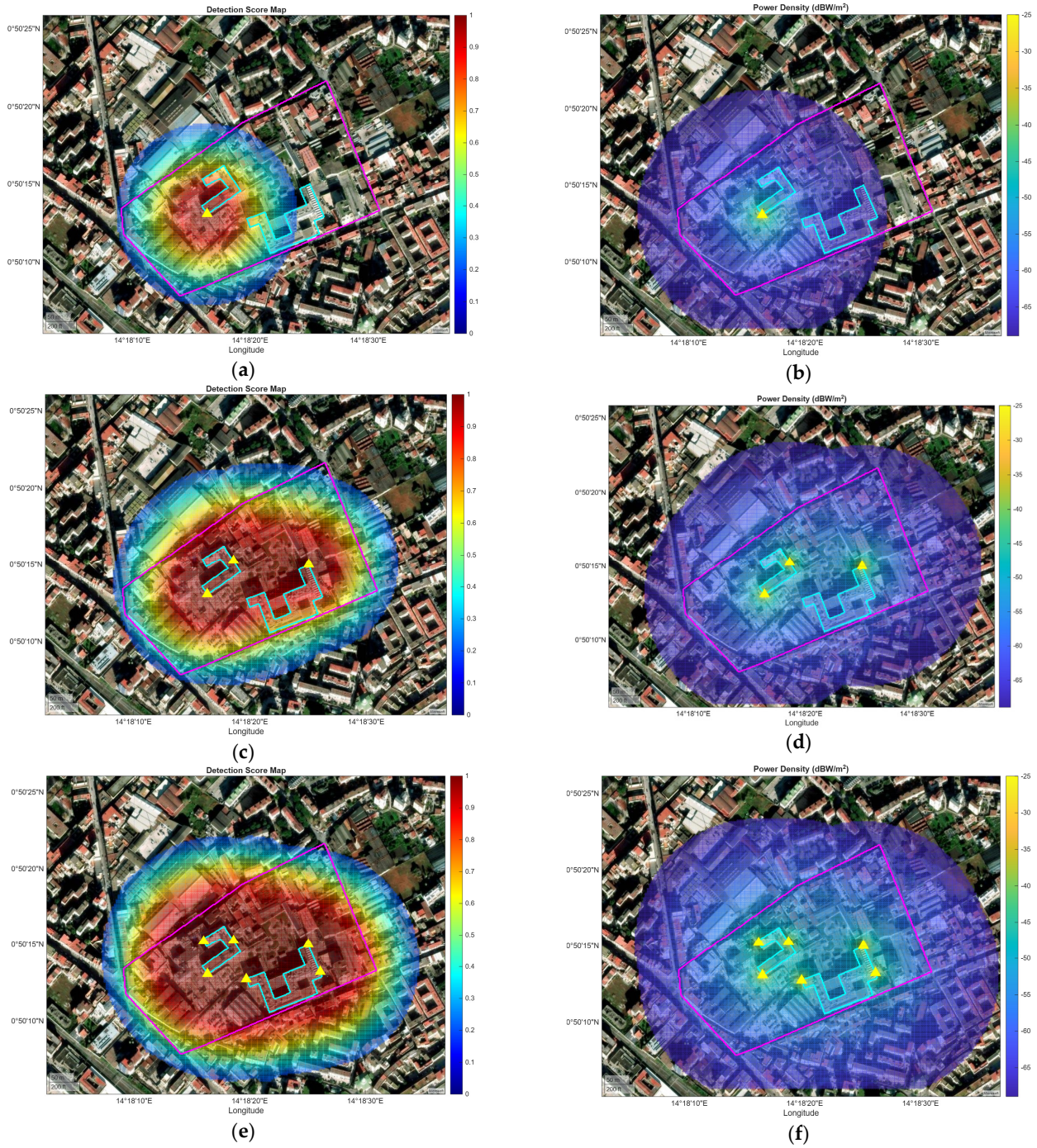

Figure 7. *Cont.*

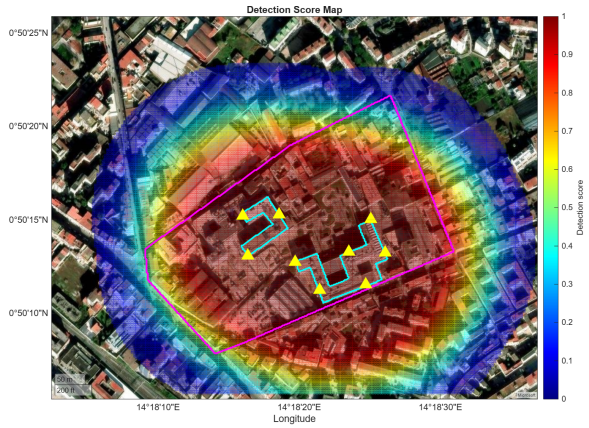

(**g**)

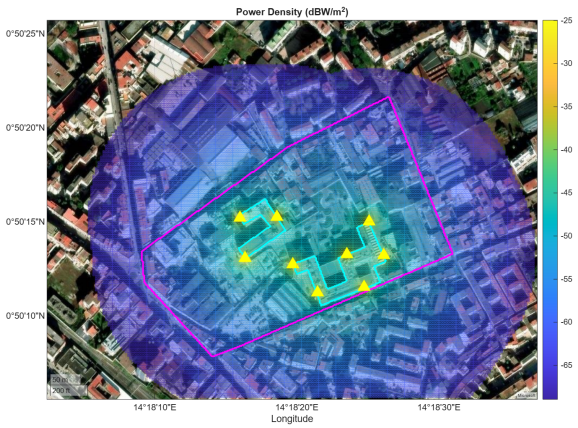

(**h**)

Figure 7. Detection-score and power-density maps respectively for: (**a**,**b**) $K = 1$, (**c**,**d**) $K = 3$, (**e**,**f**) $K = 6$, (**g**,**h**) $K = 9$.

The results show a clear increase in surveillance performance when moving from $K = 1$ to $K = 6$. The largest gain is obtained when moving from $K = 1$ to $K = 3$, with weighted coverage increasing from 30.31% to 78.92%. Further improvements are obtained for $K = 6$, reaching approximately 93.03% weighted coverage. Beyond this point, additional radar nodes provide only marginal gains, indicating the onset of a coverage-saturation effect.

This behaviour can also be observed in the detection-score maps. The central portions of the area of interest rapidly achieve high detection scores as additional radar nodes are deployed, whereas the remaining uncovered regions are mainly located near the outer boundaries of the surveillance area, where the detection score remains below the adopted coverage threshold. Consequently, increasing the radar budget beyond six nodes produces only limited improvements in the overall coverage metric.

From an exposure perspective, both the mean and the 95th-percentile power-density values increase with the number of deployed radars, as expected from the additive contribution of multiple radar nodes. Nevertheless, the exposure field remains strongly localized around the installation sites, while substantially lower power-density levels are observed throughout the majority of the monitored area. The use of a fixed colour scale for all power-density maps enables direct comparison between deployment configurations and highlights the trade-off between surveillance performance and electromagnetic exposure.

7.2. Sensitivity to Kernel Parameters

To assess sensitivity to the surrogate-model assumption, the Gaussian standard deviation σ was varied while the nominal radar budget was fixed at $K = 6$. For each σ, the code regenerates the truncated kernel and independently reruns the greedy placement.

The parameter σ was varied from 60 m to 140 m, spanning narrower and broader profiles around the reference value $\sigma = 100$ m. For each configuration, weighted coverage, mean power density, and the 95th-percentile power density are computed by the code using the same procedures described above, although Table 5 currently reports only weighted coverage and mean power density.

The results show that the surrogate sensing-kernel width has a significant impact on surveillance performance. For smaller values of σ, the sensing-score field is more concentrated around the radar locations, leading to lower overlap between neighbouring sensors and reduced coverage of the area of interest. As σ increases, the sensing-score field becomes progressively broader, resulting in a substantial increase in weighted coverage.

The most significant improvements are observed between $\sigma = 60$ m and $\sigma = 100$ m, where the weighted coverage increases from approximately 45% to 93%. Further increases

in σ continue to improve coverage, although with progressively smaller gains, reaching approximately 99% for $\sigma = 140$ m.

Table 5. Sensitivity of weighted coverage and mean power density to the Gaussian kernel width for $K = 6$.

Kernel σ (m)	Weighted Coverage (%)	Mean Power Density ($\mu W/m^2$)
60	45.738	2.681
80	69.903	2.681
100	93.034	2.683
120	98.416	2.682
140	99.827	2.683

Mean power density remains nearly unchanged across the investigated σ values because transmitted power and radar count remain fixed; small changes arise because the greedy optimizer may select different sites.

The sensitivity results indicate that larger σ values broaden the surrogate sensing-score field, while exposure changes only through the selected radar locations.

8. Discussion

The results show that, under the adopted surrogate-modelling assumptions, effective surveillance of complex environments can be improved not only by increasing the number of sensors, but also by aligning their placement with spatial surveillance priorities. By incorporating the interest-weighted map into the planning process, the proposed framework is able to concentrate higher normalized sensing scores in areas with higher operational value, avoiding configurations driven solely by uniform spatial coverage.

This behavior is particularly relevant to AAM and U-space scenarios, in which surveillance requirements are often spatially heterogeneous and concentrated along predefined corridors, approach and departure paths, or around specific assets. In such cases, uniform geographical coverage may lead to inefficient use of sensing resources, whereas a priority-driven deployment can concentrate radar coverage where unauthorized or non-cooperative UAV activity is most relevant. The proposed framework may therefore support applications such as the protection of vertiports and airport perimeters, the monitoring of urban corridors used for package-delivery operations, and the surveillance of industrial facilities or critical infrastructure.

From a planning perspective, the framework provides a decision-support layer for comparing alternative radar-network configurations under user-defined siting constraints and scenario-specific priority maps. The results also indicate that increasing the radar budget beyond a certain point produces progressively smaller improvements in weighted coverage. This suggests that, for the considered scenario, placement strategy and spatial prioritization may be as important as the total number of deployed sensors. Moreover, the minimum inter-radar spacing constraint prevents unrealistic clustering and ensures that the resulting configurations remain compatible with the available installation areas.

The integration of electromagnetic exposure screening supports the comparison of candidate deployment layouts during the planning phase. The reported power-density values should be interpreted as comparative indicators under the adopted modelling assumptions.

In conclusion, the framework should be interpreted as a flexible tool for supporting early-stage deployment decisions, rather than as a calibrated radar-performance predictor. Its main value lies in combining geospatial constraints, normalized sensing-score evalua-

tion, greedy placement optimization, and exposure screening within a single documented workflow for scenario exploration.

9. Conclusions

This study presents a planning framework for low-power ground radar networks in dense and operationally constrained environments, such as airports, seaports, and intermodal hubs. By integrating polygonal installation constraints, interest-weighted surveillance objectives, a surrogate sensing kernel, a heuristic greedy-placement procedure, and first-order exposure screening, the proposed system enables operators to identify radar deployment strategies that are effective under the adopted planning assumptions. The normalized surrogate sensing-score model provides a compact representation of range-dependent surrogate sensing effectiveness and overlapping sensor contributions, while avoiding dependence on a specific radar hardware implementation or calibrated detection chain.

Application of the system to a representative campus scenario illustrated its use as an early-stage planning tool. The results highlighted clear trade-offs between the number of deployed sensors, normalized sensing-score coverage, and exposure-screening indicators, with diminishing returns observed beyond a modest number of nodes.

Overall, the proposed methodology provides a geospatial decision-support framework for early-stage AAM surveillance planning by combining interest-weighted optimization, surrogate sensing evaluation, and electromagnetic exposure screening within a single workflow. Its flexibility allows different facility layouts and surveillance priorities to be considered while maintaining a consistent planning approach.

Future work will extend the framework by incorporating dynamic traffic patterns, more realistic sensing models, and additional constraints related to localization performance and electromagnetic exposure, further improving its applicability to operational deployment scenarios.

Author Contributions: Conceptualization, F.M., C.C. and D.A.; Methodology, C.C.; Software, F.M.; Validation, G.R.; Formal analysis, D.A.; Investigation, F.M.; Data curation, V.D.; Writing—original draft, F.M. and V.D.; Writing—review & editing, C.C., G.R. and D.A.; Visualization, V.D. and G.R.; Supervision, C.C., G.R. and D.A. All authors have read and agreed to the published version of the manuscript.

Funding: This study was carried out within the MOST—Sustainable Mobility National Research Center and received funding from the European Union Next-Generation EU (PIANO NAZIONALE DI RIPRESA E RESILIENZA (PNRR)—MISSIONE 4 COMPONENTE 2, INVESTIMENTO 1.4—D.D. 1033 17 June 2022, CN00000023).

Data Availability Statement: Data is contained within the article.

Acknowledgments: This manuscript reflects only the authors' views and opinions; neither the European Union nor the European Commission can be considered responsible for them.

Conflicts of Interest: The authors declare no conflict of interest.

References

1. Chuquitarco Jiménez, C.A.; Vico Navarro, J.; Puchol, C.C.; Balbastre, J.V. Assessment of a Performance-Based Surveillance Function in the U-Space Architecture in Low/Medium Risk U-Space Airspaces. In Proceedings of the 12th SESAR Innovation Days, Budapest, Hungary, 5–8 December 2022; Paper 2022-110.
2. Doole, M.; Ellerbroek, J.; Hoekstra, J.; Mennella, A.; Oñate, M. Drone Information Service Requirements for U-Space. In Proceedings of the 8th SESAR Innovation Days, Salzburg, Austria, 3–7 December 2018; 8p.
3. Huttunen, M.T. The U-Space Concept. *Air Space Law* **2019**, *44*, 69–90. [CrossRef]
4. RTCA. *Minimum Operational Performance Standards (MOPS) for Ground-Based Surveillance Systems (GBSS) for Traffic Surveillance*; RTCA DO-381; RTCA, Inc.: Washington, DC, USA, 2020.

5. Dulia, E.F.; Shihab, S.A.M. Designing a Surveillance Sensor Network with Information Clearinghouse for Advanced Air Mobility. *Sensors* **2024**, *24*, 803. [CrossRef]
6. Tema, E.Y.; Sahmoud, S.; Kiraz, B. Radar Placement Optimization Based on Adaptive Multi-Objective Meta-Heuristics. *Expert Syst. Appl.* **2024**, *239*, 122568. [CrossRef]
7. Wang, Z.; Wang, M.; Wu, X.; Yang, S. Multi-Node Small Radar Network Deployment Optimization in 3D Terrain. *Sensors* **2025**, *25*, 1964. [CrossRef]
8. Lei, Z.; Chen, X.; Tan, Y. A Coverage Model of FMCW Radar for Optimizing Sensor Network Deployment. *IEEE/ASME Trans. Mechatron.* **2024**, *29*, 2991–3000. [CrossRef]
9. Andersson, T.R.; Bruinsma, W.P.; Markou, S.; Requeima, J.; Coca-Castro, A.; Vaughan, A.; Ellis, A.-L.; Lazzara, M.A.; Jones, D.; Hosking, S.; et al. Environmental Sensor Placement with Convolutional Gaussian Neural Processes. *Environ. Data Sci.* **2023**, *2*, e32. [CrossRef]
10. Hu, N.; Li, Y.; Pan, W.; Shao, S.; Tang, Y.; Li, X. Geometric Distribution of UAV Detection Performance by Bistatic Radar. *IEEE Trans. Aerosp. Electron. Syst.* **2024**, *60*, 2445–2452. [CrossRef]
11. Zhu, J.; Liu, W.; Zhang, X.; Lyu, F.; Guo, Z. Antenna Placement Optimization for Distributed MIMO Radar Based on a Reinforcement Learning Algorithm. *Sci. Rep.* **2023**, *13*, 17487. [CrossRef]
12. Lombaerts, T.; Kawamura, E.; Kannan, K.; Ippolito, C.; Stepanyan, V.; Gorospe, G.; Dolph, C. Considerations for Optimal Sensor Placement for Higher Accuracy Object Localization for Urban Air Mobility. In Proceedings of the AIAA SciTech Forum, Orlando, FL, USA, 6–10 January 2025; AIAA Paper 2025-0099. [CrossRef]
13. Ko, G.-H.; Moon, S.-J.; Kim, S.-H.; Kim, J.-G.; Baek, D. Fully Integrated 24-GHz 1TX–2RX Transceiver for Compact FMCW Radar Applications. *Sensors* **2024**, *24*, 1460. [CrossRef]
14. Jin, K.; Han, S.-S.; Baek, D.; Lee, H.L. Small Drone Detection Using Hybrid Beamforming 24 GHz Fully Integrated CMOS Radar. *Drones* **2025**, *9*, 453. [CrossRef]
15. Awan, M.A.; Dalveren, Y.; Kara, A.; Derawi, M. Towards mmWave Altimetry for UAS: Exploring the Potential of 77 GHz Automotive Radars. *Drones* **2024**, *8*, 94. [CrossRef]
16. International Telecommunication Union. *Guidance for Assessment, Evaluation and Monitoring of Human Exposure to Radio Frequency Electromagnetic Fields*; Recommendation ITU-T K.91 (01/2024); ITU: Geneva, Switzerland, 2024.
17. European Telecommunications Standards Institute. *Integrated Sensing and Communications (ISAC); Use Cases and Deployment Scenarios*; ETSI GR ISC 001 V1.1.1 (2025-03); ETSI: Sophia Antipolis, France, 2025.
18. Vitiello, F.; Causa, F.; Opromolla, R.; Fasano, G. Radar/Visual Fusion with Fuse-Before-Track Strategy for Low-Altitude Non-Cooperative Sense and Avoid. *Aerosp. Sci. Technol.* **2024**, *146*, 108946. [CrossRef]
19. Liu, J.; Xu, Q.; Su, M.; Chen, W. Activity Modeling and Characterization for Airport Bird Situation Awareness Using Avian Radar Datasets. *Aerospace* **2024**, *11*, 442. [CrossRef]
20. Tang, G.; Wang, C.; Zhang, Z.; Men, S. UAV Path Planning for Container Terminal Yard Inspection in a Port Environment. *J. Mar. Sci. Eng.* **2024**, *12*, 128. [CrossRef]
21. De Kerf, T.; Sels, S.; Samsonova, S.; Vanlanduit, S. A Dataset of Drone-Captured, Segmented Images for Oil Spill Detection in Port Environments. *Sci. Data* **2024**, *11*, 1180. [CrossRef]
22. Melvin, W.L.; Scheer, J.A. (Eds.) *Principles of Modern Radar, Volume 3: Radar Applications*; SciTech Publishing: Edison, NJ, USA, 2013. [CrossRef]
23. Analog Devices. *AD9363: RF Agile Transceiver Data Sheet, Rev. D*; Analog Devices, Inc.: Wilmington, MA, USA, 2016. Available online: https://www.analog.com/en/products/ad9363.html (accessed on 27 June 2026).
24. DJI. *DJI Mavic 3M User Manual*, Version 1.0; DJI: Shenzhen, China, 2022. Available online: https://www.dji.com/downloads/products/mavic-3-m (accessed on 27 June 2026).
25. Ardoino, R.; Russo, S.; Bagnato, R.; Flagiello, N.; Di Gregorio, L.; Rossi, V. Commercial Drones Radar Cross Section Characterisation at 24 GHz with a Frequency Modulated Continuous Wave Radar. In Proceedings of the 2024 International Radar Symposium (IRS 2024), Wroclaw, Poland, 2–4 July 2024; IEEE: Piscataway, NJ, USA, 2024; pp. 114–119.
26. Gong, J.; Yan, J.; Li, D. The Radar Detection Method Based on Detecting Signal-to-Clutter Ratio (SCR) in the Spectrum. In Proceedings of the 2019 Photonics & Electromagnetics Research Symposium—Spring (PIERS-Spring), Rome, Italy, 17–20 June 2019; pp. 1876–1882. [CrossRef]
27. Kapoulas, I.K.; Hatziefremidis, A.; Baldoukas, A.K.; Valamontes, E.S.; Statharas, J.C. Small Fixed-Wing UAV Radar Cross-Section Signature Investigation and Detection and Classification of Distance Estimation Using Realistic Parameters of a Commercial Anti-Drone System. *Drones* **2023**, *7*, 39. [CrossRef]

Disclaimer/Publisher's Note: The statements, opinions and data contained in all publications are solely those of the individual author(s) and contributor(s) and not of MDPI and/or the editor(s). MDPI and/or the editor(s) disclaim responsibility for any injury to people or property resulting from any ideas, methods, instructions or products referred to in the content.